Energy Storage Materials 26 (2020) 494–502

Contents lists available at ScienceDirect

Energy Storage Materials

journal homepage: www.elsevier.com/locate/ensm

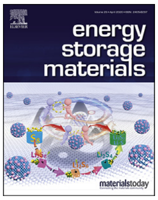

π-Conjugated polyimide-based organic cathodes with extremely-long cycling life for rechargeable magnesium batteries

Yanrong Wang [a,1], Ziteng Liu [a,1], Caixing Wang [a,1], Yi Hu [a], Huinan Lin [a], Weihua Kong [a], Jing Ma [a], Zhong Jin [a,b,*]

[a] Key Laboratory of Mesoscopic Chemistry of MOE, Jiangsu Key Laboratory of Advanced Organic Materials, School of Chemistry and Chemical Engineering, Nanjing University, Nanjing, 210023, China
[b] Shenzhen Research Institute of Nanjing University, Shenzhen, 518063, China

ARTICLE INFO

Keywords:
Multi-electron redox chemistry
Rechargeable magnesium batteries
Organic polymers
Composite cathodes
π-conjugated polyimides
Ultra-long cycling life

ABSTRACT

Rechargeable magnesium (Mg) batteries hold great promise for large-scale energy storage applications. However, the high polarity of divalent Mg^{2+} ions may induce sluggish Mg^{2+} diffusion kinetics in cathode materials, leading to inferior reversible capacity and rate performance. Herein, we report that aromatic dianhydride-derived polyimides (PIs) with reversible multi-electron redox properties can serve as advanced organic cathode materials for rechargeable Mg batteries. The π-conjugated molecular units of PIs provide abundant redox-active sites for the storage of Mg^{2+} ions, leading to large open-circuit voltage and high specific capacity. Experimental results and density functional theory (DFT) calculations of two different PI molecules indicate that the relatively narrow HOMO-LUMO energy gap and compact π-π stacking structure can help improve the Mg^{2+} storage performances. After blended with carbon nanotubes (CNTs) by in-situ polymerization and coupled with ionic liquid-modified non-nucleophilic organic electrolyte, the cathodes based on PI/CNTs composites display high rate performance, as well as impressive long-term cyclability at large current rate of 20C for over 8000 cycles. We expect this work may call forth more efforts to develop advanced organic electrode materials for rechargeable batteries based on multi-electron reactions.

1. Introduction

The soaring demands of large-scale energy storage applications are calling for efficient and economical secondary battery technologies. At present, lithium-ion batteries (LIBs) have aroused great attention from the industry [1–3]. However, lithium is subject to the limited resource, high cost, and potential safety hazard due to the dendrite formation during discharge/charge processes. Researchers are actively exploring intriguing alternative energy storage systems beyond LIBs based on monovalent and polyvalent metal ions, such as Na^+, K^+, Mg^{2+}, Ca^{2+}, Zn^{2+} and Al^{3+} [4–15]. Among them, metallic Mg possesses many advantages, such as low potential level (−2.37 V *vs.* normal hydrogen electrode, NHE), high volume specific capacity (3833 mAh cm^{-3}), abundant resource, environmental friendliness, and high safety without dendrite growth during the deposition/plating processes [16–20]. Collectively, these advantages have stimulated the research interest in the study of rechargeable magnesium batteries (RMBs). However, the strong polarization of divalent Mg^{2+} ions and the slow diffusion/migration kinetics of Mg^{2+} ions in the lattices of electrode materials seriously limit the practical performances of RMBs [21,22]. To date, only a handful of inorganic cathode materials were known to reversibly store Mg^{2+} ions, such as MnO_2 [23,24], V_2O_5 [25,26], thiospinel Ti_2S_4 [27], layered TiS_2 [28,29] and VS_4 [30]. Among them, the best-known cathode material for RMBs is Chevrel phase Mo_6S_8 [22,31,32], which has a theoretical capacity of ~130 mAh g^{-1} and a operation voltage of ~1.3 V (*vs.* Mg^{2+}/Mg), which is not adequate for high density energy storage. Therefore, it remains a challenging problem to design new cathode materials with high voltage and high capacity for RMBs [33,34].

Redox-active organic materials, in particular organic carbonyl compounds, have been considered as promising alternative electrode materials for storing Li^+, Na^+, or K^+ ions in alkali metal ion based batteries, especially in terms of the redox stability, resource sustainability,

---

[*] Corresponding author. Key Laboratory of Mesoscopic Chemistry of MOE, Jiangsu Key Laboratory of Advanced Organic Materials, School of Chemistry and Chemical Engineering, Nanjing University, Nanjing, 210023, China.

E-mail address: zhongjin@nju.edu.cn (Z. Jin).

[1] These three authors contributed equally to this work.

https://doi.org/10.1016/j.ensm.2019.11.023
Received 22 October 2019; Received in revised form 18 November 2019; Accepted 18 November 2019

environmental friendliness, light weight and low cost [35–39]. However, so far, very few organic cathode materials have been reported for the application in RMBs [40–44]. A common issue is that organic cathode materials usually only deliver low specific capacities for Mg^{2+} storage even at low current densities and suffer from considerable capacity decay upon cycling. One of the main reasons could be attribute to the serious dissolution of organic redox species in electrolytes, which has also been reported in Li^+ and Na^+ ion batteries [45–47]. Moreover, the electrical insulation of organic electrode materials also limits the kinetics of electrochemical reactions.

Herein, we report the design of organic cathode materials based on the composites of π-conjugated aromatic dianhydride-derived polyimides (PIs) and carbon nanotubes (CNTs), which demonstrate remarkable electrochemical performances for Mg^{2+} storage in ionic liquid-modified non-nucleophilic organic electrolyte. PIs, such as naphthalene-1, 4, 5, 8-tetracarboxylic acid dianhydride-ethylene diamine copolymer (termed

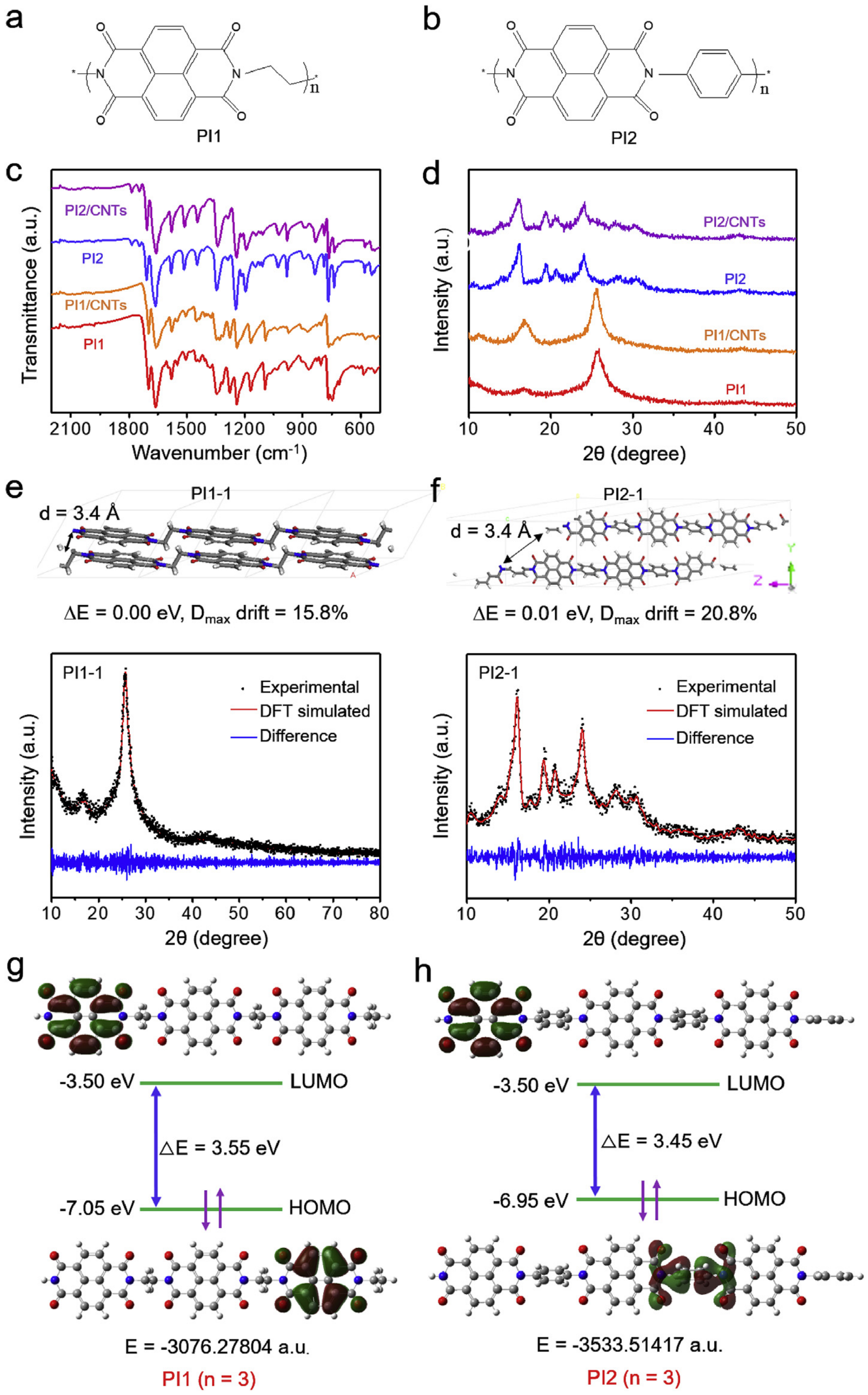

Fig. 1. (a, b) Schematic molecular structures of (a) PI1 and (b) PI2. (c) FTIR spectra and (d) XRD patterns of PI1, PI2, PI1/CNTs and PI2/CNTs, respectively. (e, f) DFT simulated possible packing structures, DFT simulated XRD patterns, and experimental XRD patterns of (e) PI1 and (f) PI2, respectively. (g, h) DFT calculated HOMO and LUMO energy levels of (g) PI1 and (h) PI2 with the polymerization degree n = 3, respectively.

as PI1, Fig. 1a) and naphthalene-1, 4, 5, 8-tetracarboxylic acid dianhydride-p-phenylenediamine copolymer (termed as PI2, Fig. 1b), are normally used as engineering plastics and possess the merits of good mechanical properties, high thermal stability, chemical resistance and low cost [48]. Although PIs are insulative, the redox-active carbonyls in their π-conjugated aromatic units are capable of storing charges reversibly. Ideally, each repeating unit of PI1 or PI2 can exhibit a reversible multi-electron redox behavior during electrochemical processes. To date, PIs have been explored as electrode materials for Li^+ and Na^+ storage, showing acceptable capacity and good cycling stability [47,49,50]. The carbonyl groups of PIs can react with Li^+ or Na^+ ions by enolization with rapid reaction kinetics [36]. However, by now, the electrochemical performances of PIs for storing Mg^{2+} ions are not fully satisfying [51,52], probably due to the incompatibility with the common nucleophilic electrolytes, such as the well-known $PhMgCl/AlCl_3$ (APC) or $n$$Bu_2Mg/EtAlCl_2$ (DCC) electrolytes [31,53,54]. Therefore, in this work, we turned to use ionic liquid-containing non-nucleophilic electrolyte based on the tetrahydrofuran (THF) solution of $Mg(HMDS)_2$-$4MgCl_2$ (HMDS: hexamethyldisilazide) and N-butyl-N-methyl-piperidinium bis((trifluoromethyl)sulfonyl)imide ($PP_{14}TFSI$) ionic liquid, which was termed as $Mg(HMDS)_2$-$4MgCl_2$/2THF-$PP_{14}TFSI$ (as detailed in the Supplementary Information). On the other hand, CNTs are known for the high electrical conductivity and excellent mechanical strength [55], it is expected that the combination of PIs and CNTs can further improve the charge transfer performances for Mg^{2+} storage.

2. Results and discussion

To demonstrate the concept of design, the composites of CNTs and two different PIs (PI1 and PI2, as shown in Fig. 1a and b for clarification) were synthesized by an in-situ polycondensation process of dianhydride and diamine precursors in the N-methylpyrrolidone (NMP) dispersion of CNTs, as detailed in the Supplementary Information. As control samples, pristine PI1 and PI2 without the addition of CNTs were also prepared. The compositions of PI1, PI2, PI1/CNTs and P2/CNTs samples were identified by Fourier transform infrared (FTIR) spectra (Fig. 1c), and the assigned characteristic FTIR bands are listed in Table S1. The IR absorption bands of imide groups are found from all of the samples (Fig. 1c), suggesting the successful synthesis of the target products [49, 56]. The powder X-ray diffraction (XRD) patterns of the samples are shown in Fig. 1d, which are consistent with the previous report [57]. The possible packing structures of PI1 and PI2 were invesitgated and optimized by density functional theory (DFT) simulation (Fig. 1e, f and Fig. S1), and the comptational details are provided in the Supplementary Information. Briefly, there are two possible packing structures for PI1 (denoted as PI1-1 and PI1-2), and three for PI2 (denoted as PI2-1, PI2-2 and PI2-3). Among them, PI1-1 and PI2-1 are calculated to be the optimized packing structures with minimum energy levels. Moreover, simulated XRD patterns based on the optimized packing structures were also obtained by Pawley refinement, as shown in Fig. 1e and f. The D_{max} drift represents the deviation ratio of the DFT-simulated XRD result to the experimentally-obtained XRD result. There are only small differences between the experimentally-obtained XRD patterns and DFT simulated results, which well support the proposed π-π stacking structures of PI1 and PI2. Specifically, PI1-1 has the lowest energy level with a layer-by-layer stacking distance of ~3.4 Å. For the optimal stacking structures of PI2 system, PI2-1 and PI2-2 are almost energetically comparable, with a relative energy difference (ΔE) of only 0.01 eV. They present different packing modes with similar layered stacking distances of about 3.4 Å and 3.5 Å, respectively; but they possess different structural parameters: PI2-1 ($a/b/c$ = 11.1/27.3/12.7 Å, $\alpha/\beta/\gamma$ = 12.8/88.1/96.1°) and PI2-2 ($a/b/c$ = 13.9/16.6/83.7 Å, $\alpha/\beta/\gamma$ = 88.4/102.5/88.5°). Besides, PI2-3 is energetically instable with a relative energy difference of ~0.95 eV higher than PI2-1 and PI2-2. The energy levels of the lowest unoccupied molecular orbital (LUMO) and the highest occupied molecular orbital (HOMO) of PI1 and PI2 with different polymerization degrees ($n = 1, 2, 3$) are calculated, as shown in Fig. 1g, h and Fig. S2. Both PI1 and PI2 with the polymerization degree of 2 or 3 show the HOMO-LUMO gaps lower than PI1 and PI2 with polymerization degree of 1. In this study, PI2 always shows the HOMO-LUMO gap lower than PI1 with the same polymerization degree, indicating the better electronic conductivity of PI2, which is conducive to the electrochemical performance and utilization ratio for Mg^{2+} storage. The experimental results have shown that each PI2 unit can effectively store more charges than PI1 unit. In addition, we also calculated the density of different packing structures of PI1 and PI2 (Table S2). It reveals that the density is positively correlated with the packing compactness. Therefore, it's easier for Mg^{2+} intercalation into the PI2 compared with PI1, which results in the higher specific capacity of PI2/CNTs electrode.

Scanning electron microscopy (SEM) images of pristine PI1 and PI2 samples are shown in Fig. S3, revealing the nanosheet-like morphology originated from the compact laminate π-π stacking structures. Moreover, the SEM and transmission electron microscopy (TEM) characterizations of PI1/CNTs and PI2/CNTs composites in Fig. S4 show that the PI1 and PI2 nanosheets are interconnected by randomly distributed CNTs, forming 3D cross-linked conductive networks. The insets in Figs. S4c and S4d exhibit the graphitic layers of CNTs. In both composites, flake-like laminar packing structures of PI1 and PI2 can be observed, which is consistent with the above theoretical simulation results. The thermal stability of samples was investigated by thermogravimetric-differential scanning calorimeter (TGA-DSC) analysis. As shown in the TGA and DSC curves in Fig. S5, all of the samples exhibit good thermal stability without obvious weight loss when the temperature is <400 °C, which is beneficial to the high-temperature performance of RMBs.

In theory, each repeating unit of PIs can store multiple charges through a reversible redox process (Fig. 2a and b). To examine the electrochemical performance for Mg^{2+} storage, we first evaluated the compatibility of non-nucleophile $Mg(HMDS)_2$-$4MgCl_2$/2THF-$PP_{14}TFSI$ electrolyte with Mg foil in RMBs (Fig. S6), which exhibited a high decomposition voltage as high as ~2.8 V. To verify the good interfacial compatibility of $Mg(HMDS)_2$-$4MgCl_2$/2THF-$PP_{14}TFSI$ electrolyte with organic compound PI cathodes, EIS analysis of pristine PI2 cathodes in electrolytes APC was also conducted, as shown in Fig. S7a. Apparently, Charge transfer impedance of PI2 in electrolytes $Mg(HMDS)_2$-$4MgCl_2$/2THF-$PP_{14}TFSI$ is smaller than that in APC. In addition, the discharge and charge capacity at current density of 0.5C (79 mA g^{-1}) in APC electrolyte is inferior to that of $Mg(HMDS)_2$-$4MgCl_2$/2THF-$PP_{14}TFSI$ (Fig. S7b). As shown in Fig. 2c and d, both the PI1/CNTs and PI2/CNTs composites showed good chemical reversibility in the cyclic voltammogram (CV) measurements using the $Mg(HMDS)_2$-$4MgCl_2$/2THF-$PP_{14}TFSI$ electrolyte. For the PI1/CNTs composite, two broad reduction peaks were observed at around 1.43 V and 0.78 V *vs.* Mg^{2+}/Mg in the 1st discharge step (Fig. 2c). Compared to the subsequent cycles, the relatively strong polarization in the 1st cycle might be caused by the presence of oxide layer on the surface of Mg anode [58,59], Subsequently, two broad oxidation peaks appeared at ~ 1.46 and 2.14 V *vs.* Mg^{2+}/Mg. The polarization gradually diminished in the following cycles. During the 3rd cycle, a reduction peak emerged at ~1.60 V and an oxidation peak appeared at ~2.12 V *vs.* Mg^{2+}/Mg. The intensities of reduction and oxidation peaks in the first few cycles slightly decreased, possibly related to the slight swelling/dissolution of oligomeric PIs in THF-based electrolyte. For PI2/CNTs composite, two reduction peaks were also observed at around 1.63 and 0.81 V *vs.* Mg^{2+}/Mg in the 1st discharge step (Fig. 2d). Afterwards, two oxidation peaks appeared at ~1.46 V and 2.14 V *vs.* Mg^{2+}/Mg. Similar to PI1/CNTs, visible polarization also occurred in the 1st CV cycle of PI2/CNTs composite. In the 3rd cycle, a distinct reduction peak at ~1.64 V and a weak reduction peak at ~1.08 V were emerged, and two oxidation peaks appeared at around 1.43 V and 2.12 V. In the case of the reduction process, two opposite carbonyl groups in a single PI unit may generate a radical anion and then a dianion, accompanied by the association of Mg^{2+} ion (Fig. 2a and b), while in the case of the oxidation process, the carbonyl groups are recovered and

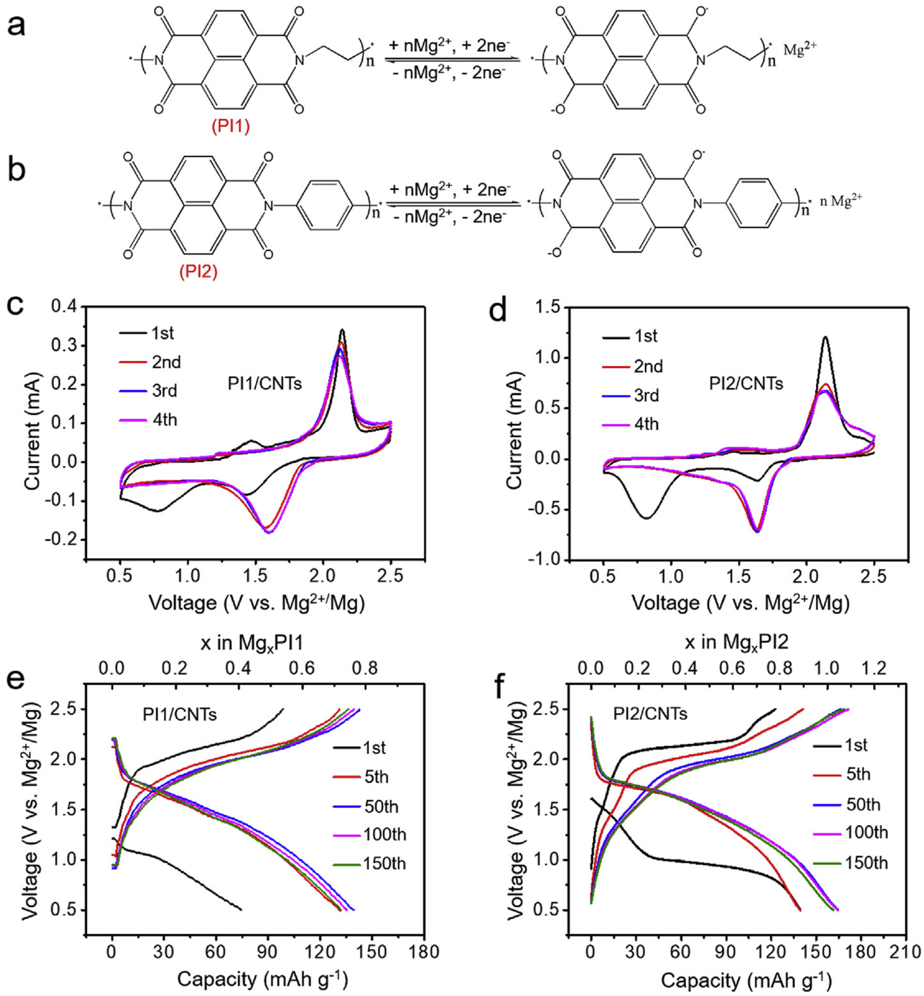

Fig. 2. (a, b) Schematic diagrams of the proposed reversible multi-electron electrochemical redox processes of (a) PI1 and (b) PI2. (c, d) CV curves of PI1/CNTs and PI2/CNTs composites at the scan rate of 0.2 mV s^{-1}. (e, f) Discharge-charge profiles of PI1/CNTs and PI2/CNTs composites during the 1st, 5th, 50th, 100th and 150th cycles at 1C, respectively.

accompanied by the disassociation of Mg^{2+} ion. However, the anticipative two pairs of well-resolved redox peaks are not displayed in the CV curves of the PI composites, only obviously-broadened redox peaks are presented. This might be attributed to the fast transformation between the radical anions and dianions [49]. Fig. 2e and f demonstrate the discharge-charge profiles of PI1/CNTs and PI2/CNTs composites at 1C in different cycles, respectively. In the 1st cycle, relatively strong polarization was observed from both of the PI composites. During the following cycles, Both PI composites delivered an average discharge voltage around 1.45 V. Notably, an activation process was observed during the initial few cycles. For PI1/CNTs composite, the reversible discharge and charge capacities gradually increased to 132 and 131 mAh g^{-1} at 1C (183 mA g^{-1}) after 5 cycles, respectively, with a corresponding Coulombic efficiency of ~100.8%. After 50 cycles at 1C (183 mA g^{-1}), the reversible discharge and charge capacities of PI1/CNTs gradually increase and reach 140 and 143 mAh g^{-1}, respectively, corresponding to a stoichiometric ratio of approximately $Mg_{0.77}$PI1/CNTs and a Coulombic efficiency of 98.0%. The discharge and charge capacities retained 132 and 136 mAh g^{-1} after the 150 cycles respectively, with a Coulombic efficiency of ~97.1%. What's better, PI2/CNTs presented higher discharge and charge capacities of 163 and 166 mAh g^{-1} after 50 cycles at 1C (158 mA g^{-1}), respectively, corresponding to a stoichiometric ratio of $Mg_{1.03}$PI2/CNTs and a Coulombic efficiency of 98%. After 150 cycles, the discharge and charge capacities retained 161 and 168 mAh g^{-1}, respectively, with a Coulombic efficiency of ~95.8%. The atomic contents of Mg^{2+} in the PI2/CNTs composite at the end of the 50th discharge and charge steps were also estimated by energy-dispersive X-ray spectroscopy (EDX), as shown in Fig. S8, which is in good agreement with the above-measured capacities.

The electrochemical Mg^{2+} storage behaviors of pristine PI1, PI2, PI1/CNTs and PI2/CNTs cathodes in non-nucleophilic $Mg(HMDS)_2$-$4MgCl_2$/2THF-PP_{14}TFSI electrolyte were investigated. Fig. 3a presents the cycling performances of PI1 and PI1/CNTs electrodes at 1C (183 mA g^{-1}). Both electrodes showed an activation process during the first few cycles, and the polarization decreased in the subsequent cycles, which is coincident with the discharge-charge profiles in Fig. 2e. The pristine PI1 electrode showed a discharge capacity of 111 mAh g^{-1} after 150 cycles at 1C; by contrast, PI1/CNTs delivered a higher capacity of 132 mAh g^{-1} at the same conditions. The pristine PI2 and PI2/CNTs electrodes showed discharge capacities of 127 and 161 mAh g^{-1} after 150 cycles at 1C (158 mA g^{-1}), which are higher than those of PI1 samples. The rate performances of PI1/CNTs and PI2/CNTs are shown in Fig. 3c and d. The discharge capacities of PI1/CNTs composite at 1C, 2C, 4C, 10C, and 20C are 125, 100, 87, 73 and 59 mAh g^{-1}, respectively. The discharge capacity at 20C of PI1/CNTs remained 47% of that at 1C. The capacity recovered back to 93 mAh g^{-1} when the current rate was reduced to 2C. Similarly, the discharge capacities of PI2/CNTs composite at 1C, 2C, 4C, 10C, and 20C are 161, 140, 118, 84 and 63 mAh g^{-1}, respectively. The discharge capacity of PI2/CNTs at 20C remains 39% of that at 1C, and turned back to 136 mAh g^{-1} when the current rate was decreased to 2C. Coulombic

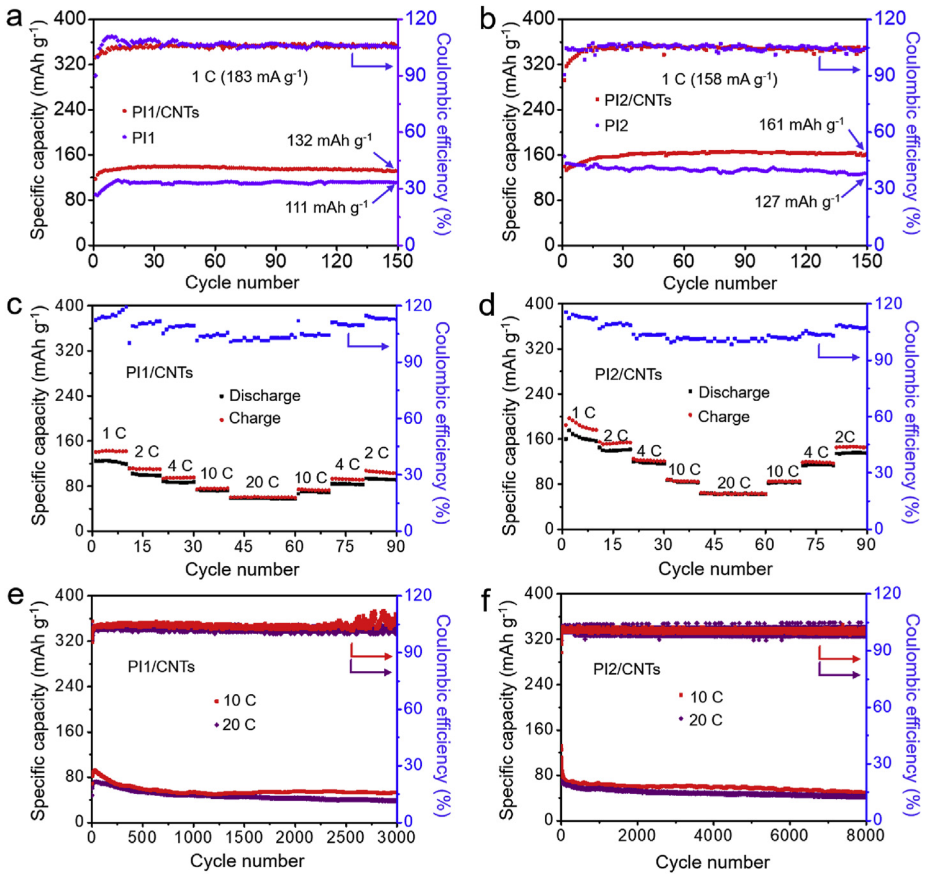

Fig. 3. (a, b) Cycling performances of pristine PI1, PI2, PI1/CNTs and PI2/CNTs cathodes at the current rate of 1C. (c, d) Rate performances of PI1/CNTs and PI2/CNTs cathodes at different rates ranged from 1C to 20C. (e, f) Long-term cycling tests of PI1/CNTs and PI2/CNTs cathodes at 10C and 20C, respectively.

efficiency at low current (Fig. 3c and d) is worse than that of high rate, which could be caused by self-discharge of battery. Self-discharge of battery is worse at lower current density than that of high rate, leading to deviation of *Coulombic efficiency* from 100%, which has been reported in the previous work about Mg batteries [60]. In addition, the electrochemical performance of PI2/CNTs composites at mass loading of 2–3 mg cm^{-2} is also provided in Fig. S9. As control samples, the Mg^{2+} storage properties of pristine PI1 and PI2 were also investigated (Fig. S10), which are inferior to those of PI1/CNTs and PI2/CNTs.

The long-term cycling stability of PI1/CNTs and PI2/CNTs cathodes in RMBs at high current rates of 10C and 20C are displayed in Fig. 3e and f. The periodical capacity fluctuation during the cycling processes could be ascribed to the room-temperature difference between day and night. The PI1/CNTs cathodes delivered 52 and 39 mAh g^{-1} after 3000 cycles at 10C and 20C, respectively. The PI2/CNTs composite cathodes delivered 61 and 50 mAh g^{-1} after 3000 cycles at 10C and 20C, and still retained 48 and 42 mAh g^{-1} after 8000 cycles, respectively. To the best of our knowledge, these results indicate the record-breaking cycling stability of PI/CNTs composites among the existing organic electrode materials for RMBs [41,42,60].

To confirm the favorable effect of CNTs to the charge transfer, the CV curves and electrochemical impedance spectroscopy (EIS) analysis of pristine PI1, PI2, PI1/CNTs and PI2/CNTs cathodes were compared, as shown in Fig. S11. The increased current intensities and lower resistance values of PI1/CNTs and PI2/CNTs could be attributed the improved conductivity originated from the presence of cross-linked CNT networks. The electrochemical equivalent circuit model for fitting Nyquist plots for all cathodes is shown in Figs. S11c and d, both PI1/CNTs and PI2/CNTs display much decreased impedance compared with the PI1 and PI2. The electrode reaction kinetics of PI2/CNTs was systematically investigated by CV at different sweep rates from 0.2 to 2.0 mV s^{-1} (Fig. 4a). In theory, the voltammetric response of an electrode-active material at various sweep rates can be evaluated as following [61–63].

$$i(\mathrm{V}) = av^{b} \tag{1}$$

$$\log i(\mathrm{V}) = b\log v + \log a \tag{2}$$

where the measured current (i) obeys a power law relationship with the sweep rate (v), a and b are the adjustable parameters. For an electrochemical system predominated by the diffusion process, the peak current i varies as $v^{1/2}$ (that is, $b = 0.5$); for a capacitive-controlled process, i varies as v (that is, $b = 1$). The CV curves of PI2/CNTs cathode exhibit two pairs of broad cathodic and anodic responses (Fig. 4a). The relationship between log(i) (at each peak current) and log(v) are shown in Fig. 4b. The b-value determined by the slopes of the four redox peaks are 0.58, 0.94, 0.99, and 0.52, implying that the capacity of PI2/CNTs is contributed by the both diffusive and capacitive processes. The CV curves of pristine PI1 and PI2 at various scan rates from 0.2 to 2.0 mV s^{-1} and their relationships between log(i) (at each peak current) and log(v) are also provided in Fig. S12, which show similar trends. Furthermore, the respective current contributions from the capacitance effect (k_1v) and intercalation process ($k_2v^{1/2}$) can be calculated according to the following equation [62,64].

$$i(\mathrm{V}) = k_1v + k_2v^{1/2} \tag{3}$$

$$i(\mathrm{V})v^{-1/2} = k_1v^{1/2} + k_2 \tag{4}$$

At a particular voltage, the k_1v represents the capacitive-controlled current and $k_2v^{1/2}$ corresponds to the diffusion-limited current. For instance, in the CV curve scanned at 0.2 mV s^{-1} (Fig. 4c), the ratio of stored charges contributed by the capacitive current is about 50%

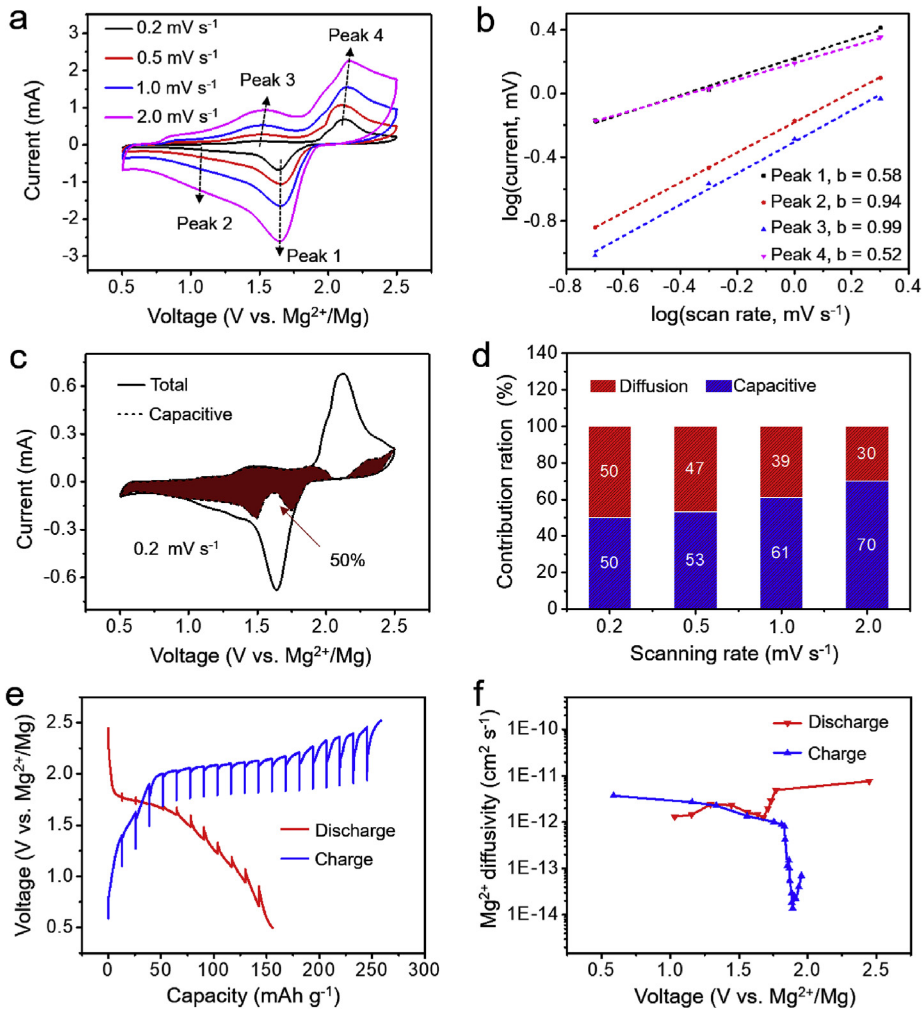

Fig. 4. Electrochemical reaction kinetics of PI2/CNTs electrode. (a) CV curves of PI2/CNTs electrode at various scan rates from 0.2 to 2 mV s-1 in the potential range of 0.5–2.5 V. (b) Power law dependence of measured currents on the scan rates at corresponding peak potentials calculated by the equation: log i(V) = b log v + log a. (c) CV curve scanned at 0.2 mV s^{-1} with the capacitive contribution (the shaded region) calculated based on the equation: i(V) = k1v + k2v1/2. (d) Column charts of the rate-dependent charge storage contributions from diffusion-limited and capacitive-controlled processes. (e) GITT curves measured under a repeating constant current pulse of 0.2C (32 mA g-1) for 20 min followed by a relaxation period of 30 min. (f) Diffusivity of Mg2+ ions versus voltage during the discharge and charge processes calculated based on GITT curves.

(corresponding to the shaded area). The contribution ratios of capacitive process at other scan rates of 0.5, 1.0, and 2.0 mV s^{-1} are calculated to be 53%, 61%, and 70%, respectively, as shown in Fig. 4d. The results show that the capacitive contribution in the total capacity at small scan rates of 0.2 mV s^{-1} is comparable to the diffusion-limited contribution. As the scan rate increases, the capacitive contribution ratio will be further improved, which is responsible for the good rate performance of PI/CNTs electrodes in RMBs.

The diffusivity coefficient of Mg^{2+} ions (D_{Mg2+}) is one of the most important influence factors for Mg^{2+} storage performance. Galvanostatic intermittent titration technique (GITT) was employed to analyze the D_{Mg2+} in PI2/CNTs cathode. In Fig. 4e, the PI2/CNTs cathode delivered the discharge and charge capacities of 156 mAh g^{-1} and 252 mAh g^{-1} in the GITT measurement, respectively. Fig. S13b shows the linear relationship between the cell voltage and the square root of τ, which indicates that D_{Mg2+} can be calculated from the potential response to the small constant current pulse (0.1C) according to the following equation [65,66].

$$D_{Mg^{2+}} = \frac{4}{\pi\tau}\left(\frac{m_B V_M}{M_B S}\right)^2 \left(\frac{\Delta E_s}{\Delta E_\tau}\right)^2$$

where τ refers to the constant current pulse time, m_B, V_M and M_B are the mass, molar volume, molar mass of the cathode material, and S is electrode-electrolyte interface area, respectively. $\triangle E_\tau$ is the potential change during the current pulse without IR drop, and $\triangle E_s$ is the potential difference between the equilibrium states before and after the current pulse (Fig. S13). As shown in Fig. 4f, the D_{Mg2+} of PI2/CNTs cathode before and after the discharge plateau during the discharge process was as high as $7.65*10^{-12}$ cm^2 s^{-1} and $1.31*10^{-12}$ cm^2 s^{-1}, and the D_{Mg2+} of PI2/CNTs cathode before and after the charge plateau during the charge process was determined to be $3.72*10^{-12}$ cm^2 s^{-1} and $7*10^{-14}$ cm^2 s^{-1}, respectively. Minimum D_{Mg2+} values were obtained at the plateau voltages for both the discharge ($1.27*10^{-12}$ cm^2 s^{-1}) and charge ($1.39*10^{-14}$ cm^2 s^{-1}) processes.

To investigate the possible intercalation positions of Mg^{2+} ions in the matrices of PI1 and PI2 based electrodes, DFT simulation was performed to calculate the optimized geometries of Mg^{2+} intercalated PI1 and PI2 materials with a stoichiometric ratio of 1:1 (denoted as MgPI1 and MgPI2, respectively), as shown in Fig. 5, and the corresponding relative formation energies are provided in Table S3 and Table S4, respectively. It is notable that there are several different Mg^{2+} intercalation positions for the possible stacking structures of PI1 and PI2. The calculation results indicate that the discharging processes of PI-based RMBs (corresponding to the Mg^{2+} intercalation into PI1 and PI2) are energetically favorable, being benefited from the electrostatic interactions between the Mg^{2+} ions with the C═O (or C–O$^-$) groups.

In order to gain further in-depth understanding behind the excellent cycling performances of Mg-PI1 and Mg-PI2 battery system, *ex-situ* X-ray photoelectron spectroscopy (XPS) analysis was carried out to investigate the chemical bonding and composition variations of the organic cathodes. Fig. 6a shows the high-resolution C 1s XPS spectra of pristine PI1 electrode at freshly-prepared state and after the 1st discharge/charge steps. The C 1s XPS spectrum of freshly-prepared PI1 cathode shows four

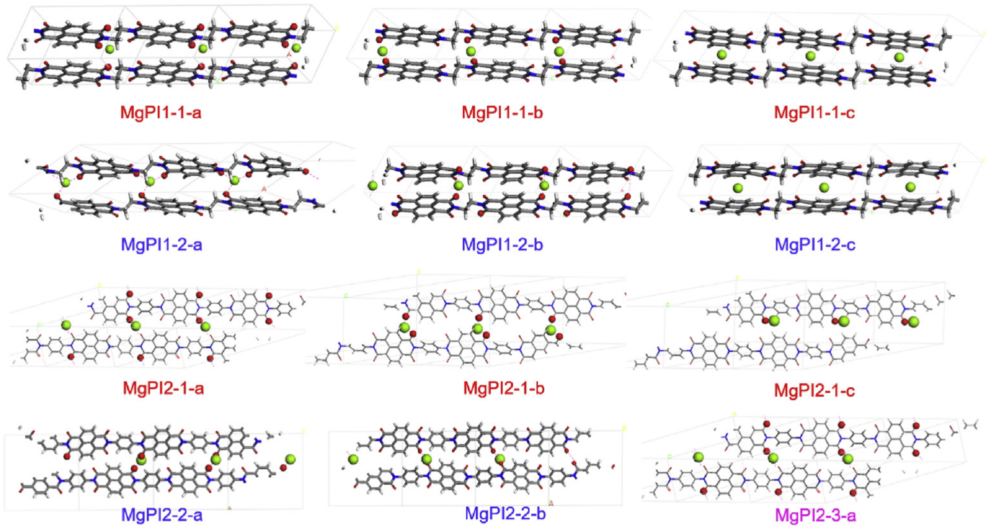

Fig. 5. The optimized geometries of MgPI1 and MgPI2 with different possible intercalation positions of Mg^{2+} ions.

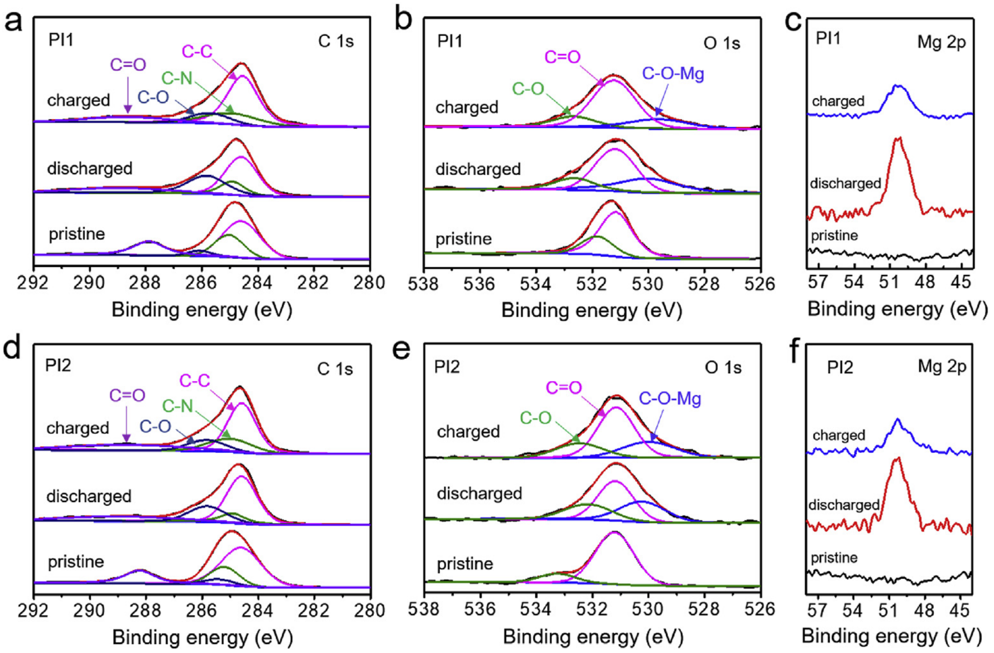

Fig. 6. *Ex-situ* XPS spectra at (a) C 1s, (b) O 1s, (c) Mg 2p regions acquired from pristine (a–c) PI1 and (d–f) PI2 cathodes at freshly-prepared state, after the 1st discharge step, and after the 1st charge step, respectively.

peaks at 284.6 eV (C–C) and 285.0 eV (C–N), 286.1 eV (C–O), and 287.9 eV (C═O), respectively. After discharged to 0.5 V, the significantly-increased intensities of C–O band at 285.8 eV and the decreased intensities of C═O band at 288.5 eV indicate the transformation of C═O to C–O–Mg during the discharge process. And the peak intensity of C–O–Mg species at 285.7 eV decreased. However, the peak of C–O–Mg didn't completely disappear, indicating that partial Mg^{2+} ions were remained in the organic cathode, which is simlar to the results in our previous work [30], and such irreversibility could explain the relatively low initial Coulombic efficiency. After recharged to 2.5 V, the peak intensity of imide C═O groups at 288.5 eV didn't completely recover, because partial Mg^{2+} ions were still remained in the PI cathode. Similarly, Fig. 6b shows the O 1s XPS spectra of pristine PI1 electrode at freshly-prepared state and after 1st charge/discharge steps. The freshly-prepared PI1 cathode was free of the characteristic peak of C–O–Mg component (around 529.9 eV) [67]. After the 1st discharge step, a strong peak of C–O–Mg appeared, suggesting the formation of C–O–Mg by the interaction of Mg^{2+} ions with C═O bonds. Subsequently, after the 1st charge step, the C–O–Mg signal in the O 1s spectrum was suppressed, indicating the recovery of carbonyl groups (C═O) from the enolate groups (C–O$^-$). The quantitative ratio variations of these species at different discharge/charge states were further evaluated by XPS analysis, as shown in Table S5. In Fig. 6c, the high-resolution Mg 2p XPS spectra of pristine PI1 electrode after the 1st discharge and charge steps show the energy band of Mg^{2+} ions located at ~50.3 eV. The intensity of Mg 2p band after the 1st discharge step is higher than that after the 1st charge step, indicating that partial Mg^{2+} ions still remained in the PI matrix after charge step. Fig. 6d–f shows the C 1s, O 1s, and Mg 2p XPS spectra of pristine PI2 electrode at freshly-prepared states and 1st discharge/charge steps, showing the variation trends of peak intensities similar to those of PI1. The quantitative ratio changes of peak intensities in the O 1s XPS spectra of pristine PI2 electrode is also summarized in Table S5. Therefore, it can be concluded that the redox mechanism of PI electrodes involves the coordination/uncoordination of Mg^{2+} ions and the reversible transformation between C=O and C–O–Mg. FTIR measurement has been conducted, shown in Fig. S14. The intensity of imide C=O stretching bands at about 1664 and 1706 cm^{-1} and imide –C–N– stretching at around 1344 cm^{-1} decrease upon discharge (A slight deviation from IR spectra of powder PI2 may be due to the influence of carbon paper current collector). And a new band emerges at 1384 cm^{-1}, which can be attributed to the stretching of –C–O–Mg^{2+} [68]. The FTIR signals (Fig. S14) in the wavelength range between 1400 and 1700 cm^{-1} also indicate that the C=O groups of the polymer can not be fully recovered after discharing and charging, owing to the interactions of C=O groups with the residual Mg^{2+} ions.

In summary, here we report that the organic cathode materials based on the composites of aromatic dianhydride-derived polyimides (PIs) and CNTs can deliver excellent electrochemical performance for Mg^{2+} storage. Benefited from the highly-reversible multi-electron redox processes of π-conjugated PIs and the 3D-crosslinked conductive networks of CNTs, the PI/CNTs cathodes exhibited high capacities and ultralong cycling stability in RMBs. The non-nucleophile Mg(HMDS)$_2$-4MgCl$_2$/2THF-PP$_{14}$TFSI electrolyte also contributed to the large voltage window and good interfacial compatibility. According to systematical electrochemistry tests, the Mg^{2+} storage capacity of PIs was attributed to the contributions of both capacitive-controlled and diffusion-limited processes. DFT simulation and *ex-situ* XPS analysis revealed the reversible conversion between C=O and C–O–Mg species during the discharge/charge cycles. We expect this work will highlight the potential of designing novel organic electrode materials with high performances, low-cost, and environmentally-benign for sustainable energy storage applications.

Declaration of competing interest

The authors declare that they have no known competing financial interests or personal relationships that could have appeared to influence the work reported in this paper.

Acknowledgements

This work was supported by National Key R&D Program of China (2017YFA0208200, 2016YFB0700600, 2015CB659300), Projects of NSFC (21872069, 51761135104, 21573108), Natural Science Foundation of Jiangsu Province (BK20180008), High-Level Entrepreneurial and Innovative Talents Program of Jiangsu Province, and the Fundamental Research Funds for the Central Universities of China (0205-14380188).

Appendix A. Supplementary data

Supplementary data to this article can be found online at https://doi.org/10.1016/j.ensm.2019.11.023.

References

[1] S. Xin, L. Gu, N.H. Zhao, Y.X. Yin, L.J. Zhou, Y.G. Guo, L.J. Wan, J. Am. Chem. Soc. 134 (2012) 18510.
[2] C.F. Zhang, H.B. Wu, C.Z. Yuan, Z.P. Guo, X.W. Lou, Angew. Chem. Int. Ed. 51 (2012) 9592.
[3] Z. Wei Seh, W. Li, J.J. Cha, G. Zheng, Y. Yang, M.T. McDowell, P.C. Hsu, Y. Cui, Nat. Commun. 4 (2013) 1331.
[4] S. Wang, X.-B. Zhang, Adv. Mater. 31 (2019) 1805432.
[5] Y.H. Zhu, Q. Zhang, X. Yang, E.-Y. Zhao, T. Sun, X.-B. Zhang, S. Wang, X.-Q. Yu, J.-M. Yan, Q. Jiang, Chem 5 (2019) 168.
[6] Y.-H. Zhu, Y.-B. Yin, X. Yang, T. Sun, S. Wang, Y.-S. Jiang, J.-M. Yan, X.B. Zhang, Angew. Chem. Int. Ed. 56 (2017) 7881.
[7] Y.-H. Zhu, X. Yang, D. Bao, X.-F. Bie, T. Sun, S. Wang, Y.-S. Jiang, X.-B. Zhang, J.-M. Yan, Q. Jiang, Joule 2 (2018) 736.
[8] J. Muldoon, C.B. Bucur, T. Gregory, Chem. Rev. 114 (2014) 11683.
[9] C. Xu, Y. Chen, S. Shi, J. Li, F. Kang, D. Su, Sci. Rep. 5 (2015) 14120.
[10] Z. Rong, R. Malik, P. Canepa, G. Sai Gautam, M. Liu, A. Jain, K. Persson, G. Ceder, Chem. Mater. 27 (2015) 6016.
[11] H. Pan, Y. Shao, P. Yan, Y. Cheng, K.S. Han, Z. Nie, C. Wang, J. Yang, X. Li, P. Bhattacharya, K.T. Mueller, J. Liu, Nat. Energy. 1 (2016) 16039.
[12] S. Gheytani, Y. Liang, F. Wu, Y. Jing, H. Dong, K.K. Rao, X. Chi, F. Fang, Y. Yao, Adv. Sci. 4 (2017) 1700465.
[13] M.C. Lin, M. Gong, B. Lu, Y. Wu, D.Y. Wang, M. Guan, M. Angell, C. Chen, J. Yang, B.J. Hwang, H. Dai, Nature 520 (2015) 325.
[14] Y. Wang, R. Chen, T. Chen, H. Lv, G. Zhu, L. Ma, C. Wang, Z. Jin, J. Liu, Energy Storage Mater 4 (2016) 103.
[15] B.Q. Li, C.X. Zhao, S.M. Chen, J.N. Liu, X. Chen, L. Song, Q. Zhang, Adv. Mater. 31 (2019) 1900592.
[16] J. Muldoon, C.B.B.G. Thomas, Angew. Chem. Int. Ed. 56 (2017) 12064.
[17] H. Yoo, I. Shterenberg, Y. Gofer, R. Doe, C.C. Fischer, G. Ceder, D. Aurbach, J. Electrochem. Soc. 161 (2014) A410.
[18] R. Zhang, C. Ling, F. Mizuno, Chem. Commun. 51 (2015) 1487.
[19] H.Y. Asl, J.T. Fu, H. Kumar, S.S. Welborn, V.B. Shenoy, E. Detsi, Chem. Mater. 30 (2018) 1815.
[20] L. Kong, C. Yan, J.-Q. Huang, M.-Q. Zhao, M.-M. Titirici, R. Xiang, Q. Zhang, Energy Environ. Mater. 1 (2018) 100.
[21] H.D. Yoo, I. Shterenberg, Y. Gofer, G. Gershinsky, N. Pour, D. Aurbach, Energy Environ. Sci. 6 (2013) 2245.
[22] E. Levi, Y. Gofer, D. Aurbach, Chem. Mater. 22 (2010) 860.
[23] T.S. Arthur, R. Zhang, C. Ling, P.-A. Glans, X. Fan, J. Guo, F. Mizuno, ACS Appl. Mater. Interfaces 6 (2014) 7004.
[24] R. Zhang, T.S. Arthur, C. Ling, F. Mizuno, J. Power Sources 282 (2015) 630.
[25] Y.W. Cheng, Y.Y. Shao, V. Raju, X.L. Ji, B.L. Mehdi, K.S. Han, M.H. Engelhard, G.S. Li, N.D. Browning, K.T. Mueller, J. Liu, Adv. Funct. Mater. 26 (2016) 3446.
[26] J. Liu, C. Chen, C. He, J. Zhao, X. Yang, H. Wang, ACS Nano 6 (2012) 8194.
[27] X.Q. Sun, P. Bonnick, V. Duffort, M. Liu, Z.Q. Rong, K.A. Persson, G. Ceder, L.F. Nazar, Energy Environ. Sci. 9 (2016) 2273.
[28] X.Q. Sun, P. Bonnick, L.F. Nazar, ACS Energy Lett 1 (2016) 297.
[29] H.D. Yoo, Y. Liang, H. Dong, J. Lin, H. Wang, Y. Liu, L. Ma, T. Wu, Y. Li, Q. Ru, Y. Jing, Q. An, W. Zhou, J. Guo, J. Lu, S.T. Pantelides, X. Qian, Y. Yao, Nat. Commun. 8 (2017) 339.
[30] Y.R. Wang, Z.T. Liu, C.X. Wang, X. Yi, R.P. Chen, L.B. Ma, Y. Hu, G.Y. Zhu, T. Chen, Z.X. Tie, J. Ma, J. Liu, Z. Jin, Adv. Mater. 30 (2018) 1802563.
[31] D. Aurbach, Z. Lu, A. Schechter, Y. Gofer, H. Gizbar, R. Turgeman, Y. Cohen, M. Moshkovich, E. Levi, Nature 407 (2000) 724.
[32] H. Sano, H. Senoh, M. Yao, H. Sakaebe, T. Kiyobayashi, Chem. Lett. 41 (2012) 1594.
[33] T. Gao, M. Noked, A.J. Pearse, E. Gillette, X.L. Fan, Y.J. Zhu, C. Luo, L.M. Suo, M.A. Schroeder, K. Xu, S.B. Lee, G.W. Rubloff, C.S. Wang, J. Am. Chem. Soc. 137 (2015) 12388.
[34] H. Tian, T. Gao, X. Li, X. Wang, C. Luo, X. Fan, C. Yang, L. Suo, Z. Ma, W. Han, C. Wang, Nat. Commun. 8 (2017) 14083.
[35] Y. Liang, Z. Tao, J. Chen, Adv. Energy Mater. 2 (2012) 742.
[36] Q. Zhao, Y. Lu, J. Chen, Adv. Energy Mater. 7 (2017) 1601792.
[37] Z. Jian, Y. Liang, I.A. Rodríguez-Pérez, Y. Yao, X. Ji, Electrochem. Commun. 71 (2016) 5.
[38] T. Sun, Z.-J. Li, X.-B. Zhang, Researcher (2018), https://doi.org/10.1155/2018/1936735.
[39] T. Sun, Z.-J. Li, H.-G. Wang, D. Bao, F.-L. Meng, X.-B. Zhang, Angew. Chem. Int. Ed. 128 (2016) 10820.
[40] H. Senoh, H. Sakaebe, H. Sano, M. Yao, K. Kuratani, N. Takeichi, T. Kiyobayashi, J. Electrochem. Soc. 161 (2014) A1315.
[41] J. Bitenc, K. Pirnat, T. Bancic, M. Gaberscek, B. Genorio, A. Randon-Vitanova, R. Dominko, ChemSusChem 8 (2015) 4128.
[42] I.A. Rodriguez-Perez, Y. Yuan, C. Bommier, X. Wang, L. Ma, D.P. Leonard, M.M. Lerner, R.G. Carter, T. Wu, P.A. Greaney, J. Lu, X. Ji, J. Am. Chem. Soc. 139 (2017) 13031.
[43] Y. NuLi, Z. Guo, H. Liu, J. Yang, Electrochem. Commun. 9 (2007) 1913.
[44] A. Vizintin, J. Bitenc, A. Kopač Lautar, K. Pirnat, J. Grdadolnik, J. Stare, A. Randon-Vitanova, R. Dominko, Nat. Commun. 9 (2018) 661.
[45] X.Y. Han, C.X. Chang, L.J. Yuan, T.L. Sun, J.T. Sun, Adv. Mater. 19 (2007) 1616.
[46] Y.L. Liang, P. Zhang, S.Q. Yang, Z.L. Tao, J. Chen, Adv. Energy Mater. 3 (2013) 600.
[47] H.-G. Wang, S. Yuan, D.-L. Ma, X.-L. Huang, F.-L. Meng, X.-B. Zhang, Adv. Energy Mater. 4 (2014) 1301651.
[48] C.E. Sroog, J. Polym. Sci. Part C (1967) 1191.
[49] Z.P. Song, H. Zhan, Y.H. Zhou, Angew. Chem. Int. Ed. 49 (2010) 8444.
[50] H.P. Wu, Q.H. Meng, Q. Yang, M. Zhang, K. Lu, Z.X. Wei, Adv. Mater. 27 (2015) 6504.
[51] X.L. Fan, F. Wang, X.X. Ji, R.X. Wang, T. Gao, S.Y. Hou, J. Chen, T. Deng, X.G. Li, L. Chen, C. Luo, L.N. Wang, C.S. Wang, Angew. Chem. Int. Ed. 57 (2018) 7146.
[52] T. Bancic, J. Bitenc, K. Pirnat, A.K. Lautar, J. Grdadolnik, A.R. Vitanova, R. Dominko, J. Power Sources 395 (2018) 25.
[53] O. Mizrahi, N. Amir, E. Pollak, O. Chusid, V. Marks, H. Gottlieb, L. Larush, E. Zinigrad, D. Aurbach, J. Electrochem. Soc. 155 (2008) A103.
[54] R. Deivanayagam, B.J. Ingram, R.S. Yassar, Energy Storage Mater 21 (2019) 136.
[55] R.H. Baughman, A.A. Zakhidov, W.A. de Heer, Science 297 (2002) 787.
[56] Y. Yin, O. Yamada, K. Tanaka, K. Okamoto, Polym. J. 38 (2006) 197.
[57] W.W. Deng, Y.F. Shen, J.F. Qian, H.X. Yang, Chem. Commun. 51 (2015) 5097.
[58] R.M. Sun, Q.L. Wei, Q.D. Li, W. Luo, Q.Y. An, J.Z. Sheng, D. Wang, W. Chen, L.Q. Mai, ACS Appl. Mater. Interfaces 7 (2015) 20902.
[59] V. Augustyn, P. Simon, B. Dunn, Energy Environ. Sci. 7 (2014) 1597.
[60] B. Pan, J. Huang, Z. Feng, L. Zeng, M. He, L. Zhang, J.T. Vaughey, M.J. Bedzyk, P. Fenter, Z. Zhang, A.K. Burrell, C. Liao, Adv. Energy Mater. 6 (2016) 1600140.

[61] T. Brezesinski, J. Wang, J. Polleux, B. Dunn, S.H. Tolbert, J. Am. Chem. Soc. 131 (2009) 1802.
[62] P. Simon, Y. Gogotsi, B. Dunn, Science 343 (2014) 1210.
[63] V. Augustyn, J. Come, M.A. Lowe, J.W. Kim, P.L. Taberna, S.H. Tolbert, H.D. Abruna, P. Simon, B. Dunn, Nat. Mater. 12 (2013) 518.
[64] K. Zhang, Z. Hu, X. Liu, Z.L. Tao, J. Chen, Adv. Mater. 27 (2015) 3305.
[65] Q.Y. An, Y.F. Li, H.D. Yoo, S. Chen, Q. Ru, L.Q. Mai, Y. Yao, Nano Energy 18 (2015) 265.
[66] F.Y. Xiong, Y.Q. Fan, S.S. Tan, L.M. Zhou, Y.A. Xu, C.Y. Pei, Q.Y. An, L.Q. Mai, Nano Energy 47 (2018) 210.
[67] H.-C. Lee, Y.-C. Huang, T.-f. Liu, W.-T. Whang, C.-G. Chao, J. Adhes. Sci. Technol. 29 (2015) 1229.
[68] A. Vizintin, J. Bitenc, A.K. Lautar, K. Pirnat, J. Grdadolnik, J. Stare, A.R. Vitanova, R. Dominko, Nat. Commun. 9 (2018) 661.